CHEMISTRY
A European Journal

Accepted Article

Title: MnO/N-doped Mesoporous Carbon as Advanced Oxygen Reduction Reaction Electrocatalyst for Zinc-air Batteries

Authors: Jieting Ding, Shan Ji, Hui Wang, Dan J. L. Brett, Bruno G. Pollet, and Rongfang Wang

This manuscript has been accepted after peer review and appears as an Accepted Article online prior to editing, proofing, and formal publication of the final Version of Record (VoR). This work is currently citable by using the Digital Object Identifier (DOI) given below. The VoR will be published online in Early View as soon as possible and may be different to this Accepted Article as a result of editing. Readers should obtain the VoR from the journal website shown below when it is published to ensure accuracy of information. The authors are responsible for the content of this Accepted Article.

WILEY-VCH

WILEY-VCH

MnO/N-doped Mesoporous Carbon as Advanced Oxygen Reduction Reaction Electrocatalyst for Zinc-air Batteries

Jieting Ding,[a] Shan Ji,*[a,b] Hui Wang,[a] Dan J. L. Brett,[c] Bruno G. Pollet,[d] and Rongfang Wang*[a]

Abstract: The development of alternative electrocatalysts exhibiting high oxygen reduction reaction (ORR) activity is vital for the deployment of large-scale clean energy devices, such as fuel cells and Zn-air batteries. N-doped carbon materials offer a promising platform for the design and synthesis of electrocatalysts due to their high ORR activity, high surface area and tuneable porosity. In this study, MnO nanoparticles entrapped N-doped mesoporous carbon compounds (MnO/NC) were developed as electrocatalysts for ORR, and their performances were evaluated in operational zinc-air batteries. It was found that the obtained carbon materials had large surface area and high electrocatalytic activity toward ORR. The carbon compounds were fabricated by using NaCl as a template via a one-pot process, which significantly simplifies the procedure for preparing mesoporous carbon materials in turn reducing the total cost. A primary zinc-air battery based upon this material exhibits an open circuit voltage (OCV) of 1.49 V, higher than conventional zinc-air batteries that use Pt/C (Pt/C cell) as the ORR catalyst (1.41 V). In our conditions, the assembled zinc-air battery delivered a peak power density of 168 mW cm^{-2} at a current density of ca. 200 mA cm^{-2}, higher than an equivalent Pt/C cell (151 mW cm^{-2} at a current density of ca. 200 mA cm^{-2}). The electrocatalytic data revealed that MnO/NC is a promising non-precious metal ORR catalyst for practical applications in metal-air batteries.

Introduction

The challenges of global warming and depleting fossil fuels have led to extensive efforts to develop advanced technologies for green energy conversion. These include fuel cells and metal-air batteries,[1] which have in common the sluggish electrocatalytic oxygen reduction reaction (ORR).[2] Indeed, the ORR acts as a bottleneck for performance due to its slow kinetics, leading to high overpotentials and reduced efficiency.[3] Usually, precious metal-based catalysts, such as Pt/C, are required to catalyze the ORR, but the scarcity and high cost of precious metals impede upon the large-scale commercialization of these technologies.[4] Significant effort has focused on the development of low-cost and non-precious metal catalysts for ORR; these include metal oxides, non-precious metals and their alloys, and carbonaceous materials.[5]

Recently, carbonaceous materials doped with heteroatoms, such as P, S and N,[6] have attracted much research interest as metal-free ORR catalysts, due to several unique advantages, namely: excellent durability, high ORR catalytic activity and ease of accessibility.[7] For example, Wong et al. reported a low-cost synthetic method to prepare N-doped graphene via heat-treating graphene oxide with polypyrrole, in turn forming a large number of N atoms in pyrrole and facilitating the formation of active sites for ORR.[8] Porous N-doped carbon materials derived from biomass were synthesized by Ji et al. who found that the ORR activity of obtained N-doped carbon materials were comparable to that of Pt/C in an alkaline medium.[2a] N-doped carbons of mesoporous structures were also developed as catalysts to enhance the electrocatalytic performance for ORR. It was found that mass transfer and desorption/removal of gases on the electrocatalyst surfaces during the electrochemical processes can be efficiently improved through the use of mesoporous structures with high surface areas.[9] Previous studies also found that combining N-doped carbon with transitional metals, or metal oxides, can significantly enhance electrocatalytic performance owing to the synergistic effects between N-doped carbon and transitional metals.[10] It is generally well-known that nanostructured materials demonstrate favorable ORR kinetics and activity due to their size effects and large surface area.[11] Manganese oxides are promising, abundant and low-cost materials for ORR, however, the low conductivity of pristine MnO$_x$ greatly limits their practical application in ORR.[12] Therefore, it could be of great significance to combine mesoporous N-doped carbon materials with manganese oxides to improve their conductivities and achieve high ORR activities. In conventional methods, porous materials are synthesized through hard template and chemical activation methods which significantly increase the cost of resulting porous materials and thus impedes upon their practical application. Therefore, it is very important to develop a simple and low-cost synthetic method to prepare porous carbon-based catalysts.

In this study, a low-cost and scalable approach, a one-pot synthesis that uses a NaCl-assisted templating method, has been developed to prepare MnO nanoparticles entrapped in

[a]   Jieting Ding, Hui Wang, Prof Rongfang Wang
       State Key Laboratory Base for Eco-Chemical Engineering, College of Chemical Engineering
       Qingdao University of Science and Technology
       Qingdao, 266042, China
        rfwang@qust.edu.cn
[b]   Prof Shan Ji
       College of Biological, Chemical Science and Chemical Engineering
       Jiaxing University
       Jiaxing, 314001, China
        jishan@mail.zjxu.edu.cn
[c]   Prof Dan J.L. Brett
       Electrochemical Innovation Lab, Department of Chemical Engineering
       University College London
       London WC1E 7JE, UK
[d]   Prof Bruno G. Pollet
       Hydrogen Energy and Sonochemistry Research Group
       Department of Energy and Process Engineering
       Norwegian University of Science and Technology (NTNU)
       Gløshaugen Kolbjørn Hejes v1B
       NO-7491, Trondheim, Norway

       Supporting information for this article is given via a link at the end of the document.

FULL PAPER

mesoporous N-doped carbon (MnO/NC) for ORR. It was found that this new synthesis method could yield mesoporous N-doped carbon materials without the use of corrosive chemicals and complicated post-treatment procedures. The obtained N-doped carbon possesses a 3-dimensional network-like shape with enormous open porous structures, and MnO nanoparticles evenly distributed in the carbon matrix. The optimized MnO/NC samples exhibited excellent electrocatalytic properties toward the ORR, comparable and even superior to the state-of-the-art commercial Pt/C in zinc-air batteries.

Results and Discussion

Figure 1 and Figure S1 schematically present the procedure of fabrication of MnO/NC using various quantities of $Mn(NO_3)_2 \cdot 4H_2O$ and precursors, in which a low-cost peptone was used as the C/N source and NaCl as a template to form the porous structure. In conventional templating methods of synthesizing porous carbon materials, hard-templates, such as zeolites or inorganic nanoparticles, need to be synthesized firstly and then removed afterwards using corrosive chemicals, which usually make the whole synthetic procedure very complicated and expensive.[13] In this study, NaCl salt was chosen as a template to form the porous structure. At high temperature, molten NaCl forms nanodroplets and penetrates the carbonizing precursor to form pores. After the pores are formed, the NaCl template can be easily removed by rinsing with water, which can significantly simplify the procedure and reduce the total cost. As shown in Figure 1, the structure and morphology of MnO nanoparticles entrapped N-doped carbons could be tuned by changing the amount of $Mn(NO_3)_2 \cdot 4H_2O$ in the precursors.
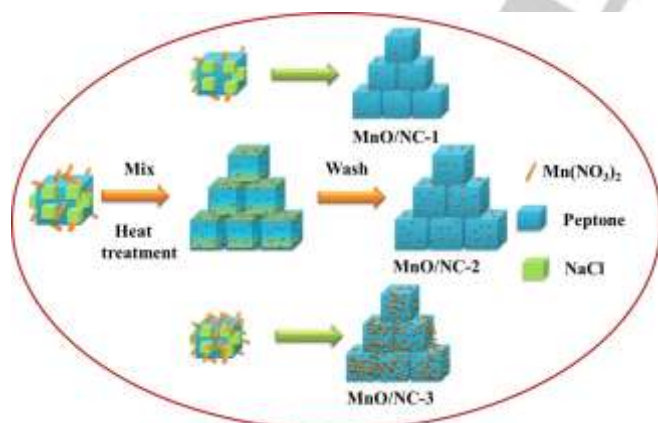

Figure 1. Schematic illustration showed the synthesis of MnO/NC-1, MnO/NC-2 and MnO/NC-3.

The morphology of the as-prepared MnO/NC samples were investigated by scanning electron microscopy (SEM), and their corresponding SEM images are presented in Figure 2. Figure 2a and b shows that MnO/NC-1 is an open structured material with a sponge-like morphology built up by interconnected thin sheets.

As seen in Figure 2c and d, MnO/NC-2 has similar morphology to MnO/NC-1. It is difficult to visually distinguish the difference between MnO/NC-1 and MnO/NC-2. However, when the quantity of $Mn(NO_3)_2 \cdot 4H_2O$ in the precursors reached 1.2 g, the sponge-like morphology almost completely disappeared, and instead thin sheet-like feature appeared, and large irregular particles were found in the SEM image of MnO/NC-3 (shown in Figure 2e). This result suggests that the carbon network structure could be damaged by the high content of $Mn(NO_3)_2$ in the precursor. Nitrates have been used as oxidizing agents for polishing diamond surfaces or for etching the inner structure of carbons, as decomposed oxygen can react with carbon atoms to form CO and CO_2.[14] Therefore, excessive amount of $Mn(NO_3)_2$ could oxidize the carbon structure, resulting in the carbon structure being damaged.
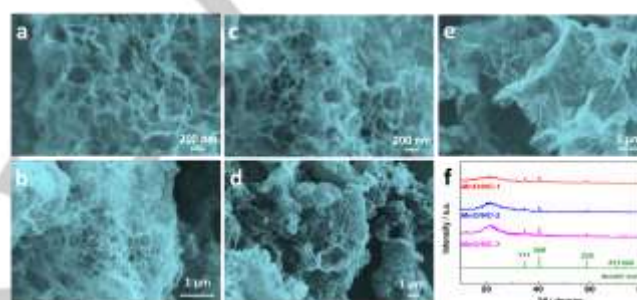

Figure 2. SEM images of MnO/NC-1(a,b), MnO/NC-2 (c,d) and MnO/NC-3 (e); XRD patterns of three samples (f).

The SEM images of the sample without $Mn(NO_3)_2$ (denoted as NC) are shown in Figure S2. The morphology of NC is similar to that of MnO/NC-2. When NaCl is absent from the reaction system, only irregular and dense blocks were observed from SEM images of the obtained samples (Figure S3), further demonstrating the the important role of NaCl in the formation of porous structure. Moreover, to reveal the effect of temperature on the structures, the samples were also synthesized at different temperatures. As shown in Figure S4, a relatively dense and solid material was obtained when the temperature was 700 ºC. At 800 ºC, foam-like structure was formed. When the temperature was increased to 900 ºC, samples containing networks with open-structure appeared. This finding indicates that the NaCl can only be used as template when the temperature is higher than 800 ºC, which could be ascribed to the fact that the melting point of NaCl is 801 ºC. When NaCl was in a molten state, the liquid-state NaCl formed nanodroplets and penetrateed the carbonizing precursor to form pores. Thus, the preparation temperature of MnO/NC samples was set at 900 ºC. The crystallinity of MnO/NC-1, MnO/NC-2 and MnO/NC-3 was studied by X-ray diffraction (XRD) analysis (shown in Figure 2f). The broad and weak hump at $2\theta \approx 24º$, attributed to the (002) plane of graphite carbon, is observed in all three XRD patterns, implying that a pseudo-graphite structure was formed.[13] Based upon the Joint Committee on Powder Diffraction Standards Card (JCPDS) No.07-0230, a well-defined XRD pattern of cubic MnO

phase was observed for all three MnO/NC samples, namely the main diffracting peaks at 34.8º, 40.6º, 58.7º, 70.2º, and 73.8º, corresponding to (111), (200), (220), (311), (222) planes of a cubic MnO phase, respectively.[15] No other forms of manganese oxides are observed in the XRD patterns, suggesting that only the cubic MnO phase was formed inside the N-doped carbon matrix. The XRD pattern of NC also shows a broad and weak peak at ca. 24º, corresponding to the graphite (002) plane (Figure S2c).
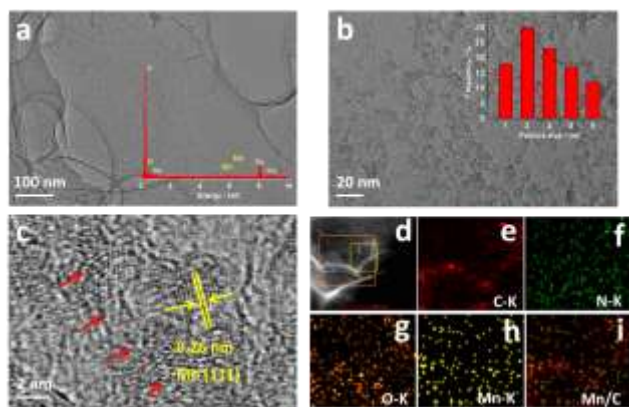

Figure 3. HRTEM images of MnO/NC-2 with inset of particle size distribution and EDX (a-c) and STEM elemental mapping analysis of MnO/NC-2 (d-i).

The microstructure of MnO/NC-2 was further evaluated by transmission electron microscopy (TEM) analysis (Figure 3). As shown in Figure 3a, a graphene-like structure is observed, which further confirms that the walls of the sponge-like structure are made up of very thin carbon nano-sheets. It is also found that there are many white small spots or pores, existed in MnO/NC-2. The EDX pattern (inset of Figure 3a) shows the signals of elements such as C, O, Cu, and Mn in the nanocomposite (the signal of Cu arises from the copper grid). Figure 3b demonstrates that irregular-shaped MnO nanoparticles are evenly distributed in the obtained N-doped carbon matrix. The average size of MnO nanoparticles was estimated about 3.7 nm from the TEM image and shown in the inset of Figure 3b (the calculation of particle size is shown in the support information section). In the high-resolution TEM (HRTEM) image of MnO/NC-2 (Figure 3c), monocrystalline lattice fringes are observed, indicating that only the pure cubic MnO phase existed in the MnO/NC-2. The lattice was measured to be 0.26 nm, indicating that the growth of MnO nanoparticles occurred preferentially on the (111) plane. The disordered fringe indicated by the red arrow could be ascribed to the graphite structure. The elemental distribution of C, N, O and Mn in MnO/NC-2 was further investigated by STEM analysis and the corresponding element mapping images are shown in Figure 3 e-i, showing that all these elements are uniformly distributed in the MnO/NC-2 sample. The corresponding TEM images of NC, MnO/NC-1 and MnO/NC-3 are also shown in Figure S5 and highlight that the thin sheet-like structure of carbon is similar to that of MnO/NC-2,

and MnO nanoparticles are uniformly dispersed on carbon. Comparing the average particle size of MnO/NC-1, MnO/NC-2 and MnO/NC-3, it was found that the amount of $Mn(NO_3)_2$ had an impact on the particle size, e.g. the average particle size increased with the increased amount of $Mn(NO_3)_2$. When $Mn(NO_3)_2$ reached 1.2 g in the precursors, much larger MnO nanoparticles, accompanied by particle aggregation, were observed in the TEM image of MnO/NC-3.

To further investigate the formation of porosity in MnO/NC samples, nitrogen (N_2) adsorption/desorption isotherms analysis (performed at 77 K) was carried out to evaluate the resulting specific surface area and pore size distribution. Based on the IUPAC classification, these isotherms shown in Figure 4a are of mixed type *I/IV*; namely, there is an obvious N_2 uptake in the relatively low-pressure region and a hysteresis loop in the relative high-pressure region, indicating that micropores and mesopores exist in these samples. In the relatively high-pressure region, all four N_2 isotherms exhibited sharp N_2 uptake due to capillary condensation, indicating the existence of macropores, which could act as a buffer for the storage of electrolyte, in turn facilitating mass diffusion during the electrocatalytic processes.[16] Pore size distributions of the four samples are presented in Figure 4b, showing that the pore sizes of these four samples are mainly centered at ca. 1.5 and 3.5 nm. The comparison between the NC and MnO/NC samples indicates the small amount of $Mn(NO_3)_2$ has little effect on the porous structure and pore size distribution of obtained carbon.
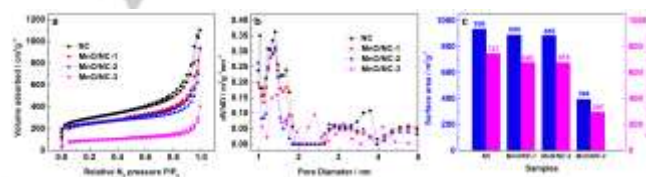

Figure 4. N_2 adsorption-desorption isotherms (a) and corresponding pore size distributions (b) of NC, MnO/NC-1, MnO/NC-2 and MnO/NC-3; (c) their corresponding BET surface area and external surface area.

The Brunauer-Emmett-Teller (BET) equation was adopted to calculate the specific surface area of NC, MnO/NC-1, MnO/NC-2 and MnO/NC-3 (presented in Figure 4c). As displayed, the BET surface area of MnO/NC-1 is slightly smaller than that of NC. Usually, the metal oxides have low BET surface areas, ranging from several to several dozen square meters per gram. For example, MnO particles prepared by pyrolysis in the presence of $Mn(NO_3)_2 \cdot 4H_2O$ precursor at 900 ºC (Figure S6) exhibited a BET surface area of 39 m^2 g^{-1}, which is only 4.2% of that of NC (936 m^2 g^{-1}). Thus, when NC was composited with MnO particles, the BET surface area per gram decreased. Inevitably, the BET surface areas of obtained MnO/NC samples decreased with the amount of MnO (as shown in Figure 4c).

Since many micropores are not accessible for the reactants, it is necessary to calculate the external surface areas, which can represent the real surface areas for electrocatalytic reactions (calculated via V-t plot method).[1e, 17] As shown in Figure 4c, the

specific surface areas and external surface areas of MnO/NC-1 and MnO/NC-2 are slightly smaller than their pure carbon counterpart. Moreover, it can be observed that there is a sharp drop in MnO/NC-3 specific surface area, which could be due to damaged carbon structure. The percentage of the external surface area/BET surface area was found to be 79.8% for NC, 76.4% for MnO/NC-1, 76.6% for MnO/NC-2, 75.4% for MnO/NC-3. The decomposition of $Mn(NO_3)_2$ will etch the carbon structure. In our conditions, at the initial pyrolysis process, $Mn(NO_3)_2$ was melted into the liquid, then reached the external surface of the intermediate. During the decomposing process of $Mn(NO_3)_2$, the carbon atom surrounding $Mn(NO_3)_2$ was oxidized, i.e. the carbon structure was etched, leading to a decrease in the external surface. These results imply that there is a need for careful introduction of $Mn(NO_3)_2 \cdot 4H_2O$ in the precursors to avoid its negative impact on the resultant porous structures.[14]
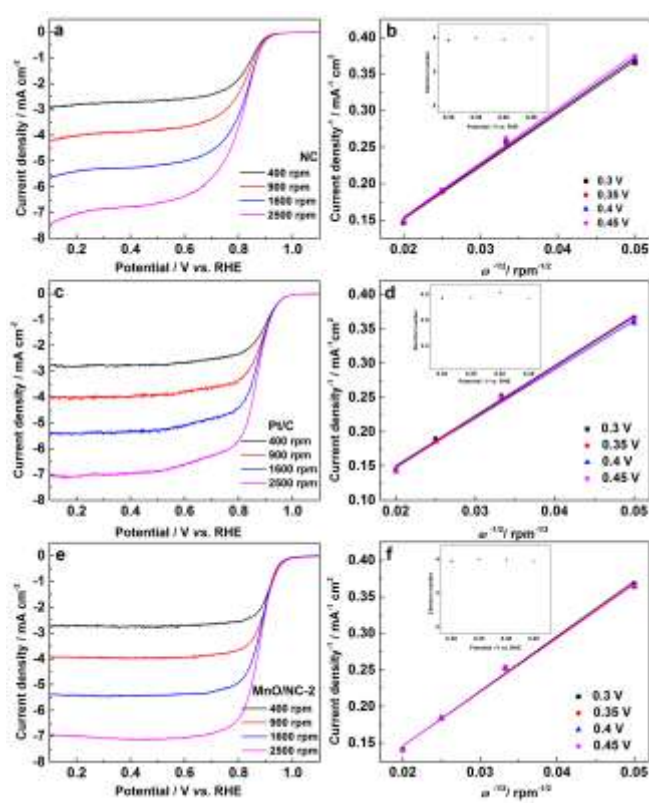

Figure 5. LSV curves of NC (a), Pt/C (c) and MnO/NC-2 (e) on RDE in O_2 saturated KOH solution at various rotation rates; and Koutecky-Levich plots of NC (b), Pt/C (d) and MnO/NC-2 (f) for ORR.

The electrochemical surface active areas of all as-prepared samples were investigated by cyclic voltammetry (CV) in 0.1 M KOH saturated with N_2. NC exhibited rectangle curves with featureless broad voltammetric responses, in agreement with the characterization of porous heteroatom doped carbon.[3a] The CV curves of MnO/NC samples had both the capacitive characteristic of NC and the redox feature of manganese oxide. The effective active surface areas of as-prepared samples were

estimated by calculating the electrochemical capacitances. Based on the CVs, the capacitances of these samples (plotted in Figure S7b) follows this order: MnO/NC-3 (31.01 F g^{-1}) < NC (33.16 F g^{-1}) < MnO/NC-1 (36.51 F g^{-1})< MnO/NC-3 (46.64 F g^{-1}), showing that introducing the small amount of MnO particles into carbon matrix can efficiently enhance the capacitance, in other words more active sites are available on the surface.

Linear sweep voltammetry (LSV) for ORR in an O_2 saturated KOH electrolyte was performed at various rotation on a rotating disc electrode (RDE) to evaluate the reaction kinetics of the NC, Pt/C, MnO/NC-1, MnO/NC-2 and MnO/NC-3 catalysts (Figure 5 and Figure S8). Their corresponding Koutecky-Levich (K-L) plots are also exhibited in Figure 5 and Figure S8. All three LSV curves show that the ORR occuring on these catalysts involved mixed processes i.e. a diffusion kinetics-controlled step in the potential range of +0.9 to +1 V vs. RHE, and a diffusion-controlled mechanism when the potential was lower than ca. +0.9 V vs. RHE. The K-L plots shown in Figure 5 are linear, indicating that the ORR occurred on these samples exhibit first-order reaction kinetics from +0.3 to +0.45 V vs. RHE.[18] The electron transfer number during the ORR was calculated according to the slope of i^1 plotted vs. $\omega^{-1/2}$. As shown by the inset of Figure 5, ORR on NC, Pt/C and MnO/NC-2 follow a four-electron pathway. However, Figure S8 shows that the ORR activity of MnO/NC-3 is much lower than that of other samples, which could be due to the low specific surface area of MnO/NC-3.
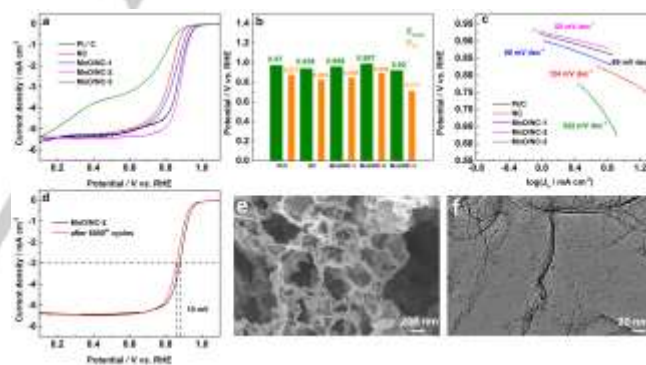

Figure 6. (a) LSV curves for ORR on different catalysts; (b) onset potential and half-wave potential for ORR on different catalysts; (c) corresponding ORR Tafel plots; (d) ORR LSV curves of the first and 6000th cycle for MnO/NC-2; (e) SEM image of MnO/NC-2 after 6000 cycles; (f) TEM image of MnO/NC-2 after 6000 cycles.

The LSV curves recorded in oxygen-saturated KOH solution at the rotating speed of 1600 rpm on these samples are compared in Figure 6a (all LSV curves presented here were subtracted from the LSVs recorded in nitrogen-saturated solution). Figure 6b shows the corresponding onset potentials and half-wave potentials for ORR, which are commonly used to judge the ORR activity. NC, MnO/NC-1 and MnO/NC-3 exhibit comparable ORR activity to Pt/C, except for MnO/NC-3. It is worthwhile noting that the onset potential and half-wave potential of MnO/NC-2 are even higher than those obtained for

the state-of-the-art commercial Pt/C. For further optimizing the ORR catalytic activity of the *as*-prepared catalysts, the MnO/NC-2 samples were prepared at different temperatures. The data shown in Figure S9 indicated MnO/NC-2 prepared at 900 °C had the highest ORR activity among all tested samples. The ORR onset potential and half-wave potential of MnO/NC-2 were also compared with some representative transitional metal-based N-doped carbon materials reported previously (Table S1). It can be ovserved that the *as*-prepared MnO/NC-2 is one of the best ORR catalysts listed in Table S1. The ORR performance of the as-prepared samples and Pt/C were further evaluated by comparing their Tafel slopes, as shown in Figure 6c. The Tafel slope of MnO/NC-2 was found to be 58 mV dec[-1], which is even lower than that of Pt/C (69 mV dec[-1]). Smaller Tafel slopes usually represent higher ORR activity. Figure 6c further confirms satisfactory electrocatalytic performance of MnO/NC-2 and its similar ORR mechanism to Pt/C.

ORR durability of MnO/NC-2 and Pt/C was investigated by cyclic voltammetry in oxygen-saturated KOH electrolyte for 6000 cycles. The first and 6000th ORR LSV curves of MnO/NC-2 and Pt/C are presented in Figure 6d and Figure S10, respectively. It can be found that the half-wave potential of MnO/NC-2 shifted negatively by 14 mV, which is much less than that of Pt/C (44 mV) after continuous 6000 cycles, indicating MnO/NC-2 has a better ORR durability than Pt/C in KOH electrolyte. The morphology of MnO/NC-2 after the durability testing was also evaluated by SEM and TEM (Figure 6e and 6f). Compared to the SEM and TEM images of fresh MnO/NC-2 (Figure 2 and 3), no visible difference can be observed after the durability testing, further confirming the structure of MnO/NC-2 is very stable in ORR testing conditions.

To evaluate the ORR performance of MnO/NC-2 under representative 'real-world' zinc-air battery conditions, the MnO/NC-2 catalyst was assembled together with Zn foil in a two-electrode primary zinc-air cell. The open circuit voltage (OCV) of MnO/NC-2 and Pt/C primary zinc-air batteries were measured versus time. As shown in Figure 7a, OCV of the MnO/NC-2 cell is higher than that of the Pt/C cell. Figure 7a also shows that both cells have stable OCV. Figure 7b presents the power density and polarization curves of the MnO/NC-2 and Pt/C cells. In the current density range of 0-200 mA cm^{-2}, the MnO/NC-2 cell has a higher cell voltage than the Pt/C cell. The MnO/NC-2 cell delivers a peak power density of 168 mW cm^{-2} at a current density of ca. 200 mA cm^{-2}, higher than the Pt/C cell (151 mW cm^{-2} at a current density of ca. 200 mA cm^{-2}), further confirming that MnO/NC-2 yields a higher power density due to its exceptional ORR electrocatalytic performance. Figure 7c shows that both MnO/NC-2 and Pt/C cells have a very stable cell voltage when discharged at 10 mA cm^{-2} for more than 20 h, and the MnO/NC-2 cell has a higher capacity than the Pt/C cell. The current responses of the MnO/NC-2 cell with increased current densities are illustrated in Figure 7d, where cell voltages gradually drop with an increase in current density. When the current density reverted to 1 mA cm^{-2}, the cell voltage returned to its initial value, indicating robustness and satisfactory rate performance of the air cathode made from MnO/NC-2. After consuming the Zn foil in the MnO / NC-2 cell, the cell was

recharged by replacing the Zn foil for six times. As shown in Figure 7e, only slight cell voltage drop is observed during the long-term galvanostatic discharge test at a current density of 10 mA cm^{-2}, further reflecting the superior ORR property and durability of MnO/NC-2 in zinc-air batteries. In order to demonstrate the outstanding capacity and stability of MnO/NC-2, two MnO/NC-2 cells were assembled and connected in series to power a 2.0 V red LED light, which was brightly lit for more than 18 h, further proving outstanding capacity and stability of the assembled cells. The electrocatalytic results clearly demonstrate that MnO/NC-2 possesses high intrinsic ORR electrocatalytic performance and excellent cell performance in real zinc-air batteries. The MnO/NC-2 is a promising alternative to noble metal-based ORR catalysts in metal-air batteries. The synergistic effects between MnO and C can enhance the charge adsorption and transfer in the electrode, showing that the introduction of a certain amount of MnO in carbon materials can efficiently improve the ORR activity.[12]
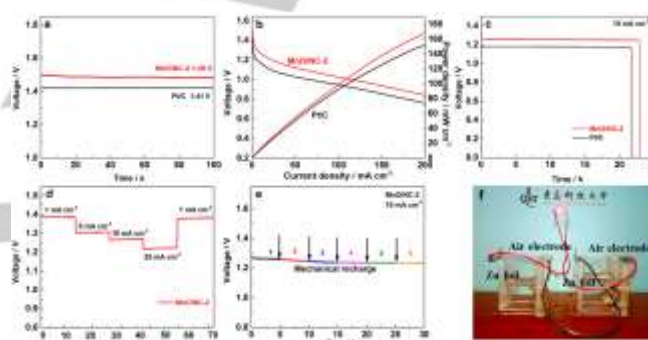

Figure 7. (a) Open circuit voltage of MnO/NC-2 and Pt/C primary zinc-air batteries; (b) Polarization and power density curves of MnO/NC-2 and Pt/C primary Zn-air batteries; (c) cell voltage vs. time at the current density of 10 mA cm^{-2}; (d) cell voltage vs. time at various current densities; (e) long-term galvanostatic discharge of MnO/NC-2 primary Zn-air battery, which had been recharged by refilling Zn foil three times; (f) Photograph of a red LED (2 V) powered by two Zn–air batteries connected in series.

For a better understanding of why MnO/NC-2 can deliver high ORR activity and durability, the surface composition and chemical state of MnO/NC-2 and NC samples were further investigated using X-ray photoelectron spectroscopy (XPS). According to Figure 8a, C, N, Mn and O elements existed in MnO/NC-2, and C, N, O elements in NC. The XPS spectrum of Mn 2p exhibits a pair of peaks at ca. 642.1 and 653.6 eV, which can be ascribed to Mn $2p_{3/2}$ and $2p_{1/2}$, matching well with a typical Mn 2p XPS spectrum of manganese oxides.[19] As illustrated in Figure 8c, C 1s XPS spectra of NC and MnO/NC-2 can be fitted into four peaks at ca. 284.8 eV, 285.6 eV, 286.3 eV and 289.1 ev, corresponding to C=C, C–O/C–N, C=O and O–C=O, respectively.[20] The presence of C-O/C-N confirmed that O and N were doped into the carbon matrix. Figure 8d shows that there are more C=O and C–O/C–N species in MnO/NC-2 than NC, suggesting the presence of these functional groups acted as active sites to catalyze the ORR. In addition, Mn acts as electron donor, which could provide electrons to the functional

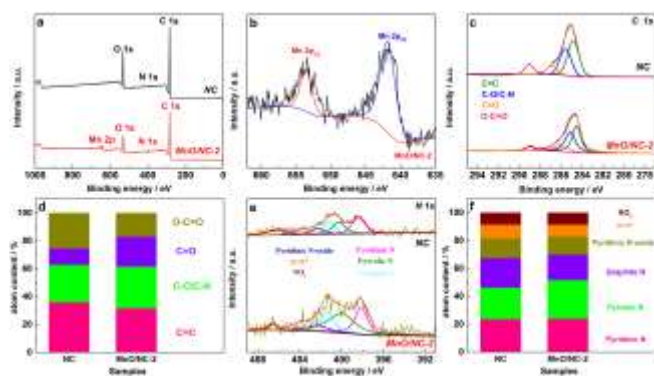group and facilitate the ORR due to the synergetic effect between Mn and C.

Figure 8. (a) XPS full spectrum of NC and MnO/NC-2; deconvoluted high resolution XPS spectra of Mn 2p (b), C 1s (c) and N 1s(e); (d) contents of C species on NC and MnO/NC-2; (f) contents of N species on NC and MnO/NC-2.

The N 1s XPS spectra of NC and MnO/NC-2 shown in Figure 8e were fitted into six peaks, showing there are six N species existing in both samples. Based on the literature,[21] the peaks at ca. 398.2 eV, 399.6 eV, 401.2 eV, 402.2 eV, 404.5 eV and 406.3 eV are attributed to pyridinic-N, pyrrolic-N, graphitic-N, pyridinic N-oxide, π-π* satellite and NOx species, respectively. Pyridinic-N provides a pair of electrons to bond with p-conjugated rings and pyrrolic-N is a good electron donor. Usually, pyridinic-N and pyrrolic-N are regarded as the active sites for electrocatalytic reactions.[22] As shown in Figure 8f, the total percentage of pyridinic-N and pyrrolic-N species in MnO/NC-2 is higher than NC, which could be the main reason why MnO/NC-2 can deliver the best ORR performance among all the as-prepared samples, even the state-of-the-art commercial Pt/C.

Conclusions

N-doped mesoporous MnO/carbon compounds of high surface area can be successfully prepared by using NaCl as a template, which can significantly simplify the procedure for preparing mesoporous carbon materials. NaCl plays a critical role in the formation of porosity and the obtained mesoporous structured carbon materials possess high specific surface areas, which could provide shortened pathways for electron and ion transfer during ORR. Due to their intrinsic electrochemical properties, the as-prepared carbonaceous materials showed outstanding electrocatalytic activity toward ORR in a KOH electrolyte. The optimized sample, MnO/NC-2, exhibited excellent ORR electrocatalytic performance, which was even higher than Pt/C in terms of ORR activity and durability. In a 'real' two-electrode primary Zn-air battery, MnO/NC cell demonstrated a high open circuit voltage of 1.49 V and high specific capacity. The low-cost of MnO/NC-2 possessing a high

ORR activity makes it a promising alternative to precious metal-based ORR catalysts for zinc-air batteries.

Experimental Section

Synthesis

0.2 g, 0.6 g and 1.2 g of $Mn(NO_3)_2 \cdot 4H_2O$ were separately mixed with 1 g of peptone powder in 15 mL of water. The aqueous solutions were freeze-dried in liquid nitrogen for 12 h. The freeze-dried mixtures were combined with 10 g of NaCl salt and ball-milled at 4000 rpm for 6 h. The milled mixtures were transferred into a tube furnace and carbonized under a nitrogen atmosphere at 900 °C for 1 h at a heating rate of 2.5 °C min^{-1}. Next, the samples were thoroughly washed with water to remove NaCl and dried at 60 °C for 12 h in a vacuum oven. The obtained samples were labelled as MnO/NC-1 (0.2 g), MnO/NC-2 (0.6 g) and MnO/NC-3 (1.2 g) based on the amount of $Mn(NO_3)_2 \cdot 4H_2O$ added to the precursors. For comparison purposes, N-doped porous carbon materials were also prepared using the same method without adding Mn precursor and labelled as "NC".

Physical Characterization

The crystallinity of the samples was characterized by X-ray diffraction (XRD) on a Shimadzu XD–3A spectrometer using filtered Cu-Kα radiation (λ = 0.15418 nm) generated at 40 kV and 30 mA. The detailed morphologies of the samples were evaluated by transmission electron microscopy (TEM) on a JEOL JEM-2000 FX instrument operating at 200 kV. Brunauer-Emmett-Teller (BET) method was employed to determine specific surface areas for obtained carbon materials, and the pore size distribution was calculated by a density functional theory (DFT) method using a slit pore NLDFT equilibrium model on a Quantachrome Autosorb-1 volumetric analyzer. X-ray photoelectron spectra (XPS) were acquired with a VG Escalab210 spectrometer fitted with a Mg 300 W X-ray source.

Electrochemical measurements

ORR electrochemical performance tests were carried out in a conventional three-electrode cell using a CHI650D electrochemical analyzer (CH Instruments). The working electrodes were prepared as follows: 5 mg of catalyst were dispersed into 1 mL Nafion ethanol solution (0.25 wt.%) by ultrasonic mixing for 30 min. 8 µL of ink containing 40 µg catalyst were dropped onto the surface of a polished glass-carbon rotating disc electrode (catalyst loading: 0.204 mg cm^{-2}) and air dried. For performance comparison, commercial Pt/C catalysts were used for the preparation of working electrodes according to the same procedure. Ag/AgCl in saturated KCl was chosen as a reference electrode and Pt wire as a counter electrode. 0.1 M KOH purged with N_2 for 30 min was used as an electrolyte for all electrochemical tests in this study. All potential values recorded in the study were converted to potentials vs. the reversible hydrogen electrode (RHE) using the following equation: $E_{RHE} = E_{Ag/AgCl} + 0.059$ pH + 0.197 V. iR curve compensation was done in the tests and ORR curves were adjusted to take capacitive effects into account.

As-prepared carbon materials were used as cathodes and Zn foil as an anode in a two-electrode cell system with 6.0 M KOH as the electrolyte. To precisely measure specific capacity, Zn foil electrodes were cut to a 1 cm^2 surface area and polished before each test. The air cathode was prepared by dispersing 2 mg of the catalyst, 3 µL of polymer binder PTFE，1 mg acetylene black and 4 mg carbon in 300 µL isopropyl alcohol to form a homogenous slurry. After rolling into a slice and oven

drying at 80 ℃, the air cathode mixture was pressed onto Ni foam under 20 MPa.

[1] a) Y. Yan, B. Xia, B. Zhao, X. Wang, *J. Mater. Chem. A* **2016**, *4*, 17587-17603; b) R. Wang, K. Wang, Z. Wang, H. Song, H. Wang, S. Ji, *J. Power Sources* **2015**, *297*, 295-301; c) T. Liu, Q. Liu, A. M. Asiri, Y. Luo, X. Sun, *Chem. Commun.* **2015**, *51*, 16683; d) Y. Ma, R. Wang, H. Wang, J. Key, S. Ji, *J. Power Sources* **2015**, *280*, 526-532; e) J. Ding, S. Ji, H. Wang, J. Key, D. J. L. Brett, R. Wang, *J. Power Sources* **2018**, *374*, 48-54.

[2] a) R. Wang, H. Song, H. Li, H. Wang, X. Mao, S. Ji, *J. Power Sources* **2015**, *278*, 213-217; b) Y. Jiao, Y. Zheng, M. Jaroniec, S. Z. Qiao, *Chem. Soc. Rev.* **2015**, *44*, 2060.

[3] a) Y. Chen, H. Wang, S. Ji, R. Wang, *Catal. Commun.* **2018**, *107*, 29-32; b) A. Sumboja, J. Chen, Y. Zong, P. S. Lee, Z. Liu, *Nanoscale* **2017**, *9*, 774-780.

[4] J. Jia, H. Wang, S. Ji, H. Yang, X. Li, R. Wang, *Electrochim. Acta* **2014**, *141*, 13-19.

[5] a) Yanguang Li, Hongjie Dai, *Chem. Soc. Rev.* **2014**, *43*, 5257-5275; b) F. Cheng, J. Chen, *Chem. Soc. Rev.* **2012**, *41*, 2172-2192; c) S. Zeng, H. Chen, H. Wang, X. Tong, M. Chen, J. Di, Q. Li, *Small* **2017**, *13*, 1700518.

[6] a) S. S. Shinde, J.-Y. Yu, J.-W. Song, Y.-H. Nam, D.-H. Kim, J.-H. Lee, *Nanoscale Horiz.* **2017**, *2*, 333-341; b) M. Zhou, H.-L. Wang, S. Guo, *Chem. Soc. Rev.* **2016**, *45*, 1273-1307.

[7] a) A. C. Martins, X. Huang, A. Goswami, K. Koh, Y. Meng, V. C. Almeida, T. Asefa, *Carbon* **2016**, *102*, 97-105; b) R. Silva, J. Al-Sharab, T. Asefa, *Angew. Chem.* **2012**, *51*, 7171-7175; c) K. Koh, Y. Meng, X. Huang, X. Zou, M. Chhowalla, T. Asefa, *Chem. commun.* **2016**, *52*, 13588-13591; d) E. H. Fragal, V. H. Fragal, X. Huang, A. C. Martins, T. S. P. Cellet, G. M. Pereira, E. Mikmeková, A. F. Rubira, R. Silva, T. Asefa, *J. Mater. Chem. A* **2017**, *5*, 1066-1077.

[8] Z. Lin, G. H. Waller, Y. Liu, M. Liu, C.-p. Wong, *Nano Energy* **2013**, *2*, 241-248.

[9] a) Z. Wang, S. Xiao, Y. An, X. Long, X. Zheng, X. Lu, Y. Tong, S. Yang, *Acs Appl. Mater. Interfaces* **2016**, *8*, 13348-13359; b) H. Li, F. Yue, C. Yang, P. Xue, N. Li, Y. Zhang, J. Wang, *Crystengcomm* **2016**, *19*, 64-71; c) R. Wang, T. Zhou, H. Li, H. Wang, H. Feng, J. Goh, S. Ji, *J. Power Sources* **2014**, *261*, 238-244.

[10] a) X. Cui, P. Ren, D. Deng, J. Deng, X. Bao, *Energy Environ. Sci.* **2016**, *9*, 123-129; b) M. Zeng, Y. Liu, F. Zhao, K. Nie, N. Han, X. Wang, W. Huang, X. Song, J. Zhong, Y. Li, *Adv. Funct. Mater.* **2016**, *26*, 4397-4404; c) Y. Xu, W. Tu, B. Zhang, S. Yin, Y. Huang, M. Kraft, R. Xu, *Adv. Mater.* **2017**, *29*, 1605957.

[11] Y. Nie, L. Li, Z. Wei, *Chem. Soc. Rev.* **2015**, *44*, 2168-2201.

[12] a) W. Xiao, D. Wang, X. W. Lou, *J. Phys. Chem. C* **2009**, *114*, 1694-1700; b) K. L. Pickrahn, S. W. Park, Y. Gorlin, H.-B.-R. Lee, T. F. Jaramillo, S. F. Bent, *Adv. Energy Mater.* **2012**, *2*, 1269-1277.

[13] Y. Chen, S. Ji, H. Wang, V. Linkov, R. Wang, *Int. J. Hydrogen Energy* **2018**, *43*, 5124-5132.

[14] a) J. Ktihnle, O. Weis, Surf. Sci. 1995, 340, 16–22; b) J. Ding, P. Wang, S. Ji, H. Wang, V. Linkov, R. Wang, *Electrochim. Acta* **2019**, *296*, 653-661

[15] a) M. Yang, Y. Zhong, X. Zhou, J. Ren, L. Su, J. Wei, Z. Zhou, *J. Mater. Chem. A* **2014**, *2*, 12519; b) S. Qiu, X. Wang, G. Lu, J. Liu, C. He, *Mater. Lett.* **2014**, *136*, 289-291.

[16] T. Ouyang, K. Cheng, Y. Gao, S. Kong, K. Ye, G. Wang, D. Cao, *J. Mater. Chem. A* **2016**, *4*, 9832-9843.

[17] J. Ding, S. Ji, H. Wang, B. G. Pollet, R. Wang, *Electrochim. Acta* **2017**, *255*, 55-62.

[18] S. Guo, S. Zhang, L. Wu, S. Sun, *Angew. Chem. Int. Ed. Engl.* **2012**, *51*, 11770-11773.

[19] Q. Gan, H. He, K. Zhao, Z. He, S. Liu, *Electrochim. Acta* **2018**, *266*, 254-262.

[20] A. Mulyadi, Z. Zhang, M. Dutzer, W. Liu, Y. Deng, *Nano Energy* **2017**, *32*, 336-346.

[21] a) H. Liu, Y. Zhang, R. Li, X. Sun, S. Désilets, H. Abou-Rachid, M. Jaidann, L.-S. Lussier, *Carbon* **2010**, *48*, 1498-1507; b) R. Arrigo, M. Havecker, R. Schlogl, D. S. Su, *Chem. Commun.* **2008**, 4891-4893.

[22] a) Y. Qiu, X. Zhang, S. Yang, *Phys. Chem. Chem. Phys.* **2011**, *13*, 12554-12558; b) D. Hulicova-Jurcakova, M. Kodama, S. Shiraishi, H. Hatori, Z. H. Zhu, G. Q. Lu, *Adv. Fun. Mater.* **2009**, *19*, 1800-1809.

FULL PAPER

WILEY-VCH

FULL PAPER

In this study, MnO nanoparticles entrapped N-doped mesoporous carbon compounds (MnO/NC) are developed as electrocatalysts for ORR, and their performance is evaluated in operational zinc-air batteries. The assembled zinc-air battery delivers a peak power density of 168 mW cm^{-2} at a current density of ca. 200 mA cm^{-2}, higher than an equivalent Pt/C cell (151 mW cm^{-2} at a current density of ca. 200 mA cm^{-2}).
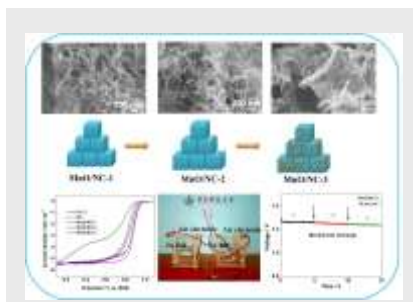
Jieting Ding, Shan Ji,* Hui Wang, Dan J. L. Brett, Bruno G. Pollet, Rongfang Wang*

MnO/N-doped Mesoporous Carbon as Advanced Oxygen Reduction Reaction Electrocatalyst for Zinc-air Batteries